

www.acsami.org Research Article

# pH-Responsive Rhodamine Nanotube Capable of Self-Reporting the Assembly State

Ziyuan Meng,<sup>†</sup> Sagarika Taneja,<sup>†</sup> Reham Hassan, and Jon R. Parquette\*



Cite This: ACS Appl. Mater. Interfaces 2024, 16, 47089–47099



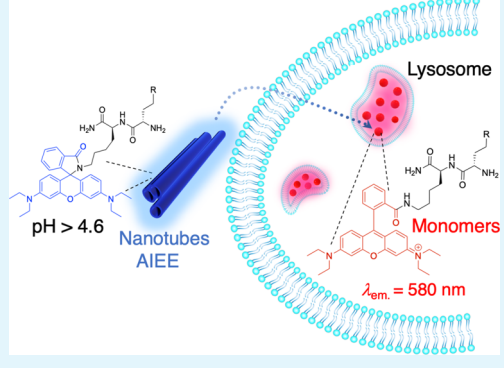
**ACCESS** I

Metrics & More

Article Recommendations

s Supporting Information

ABSTRACT: Nanomaterials that respond to intracellular signals, such as pH, have the potential for many biomedical applications, such as drug delivery, because the assembly/disassembly process can be tailored to respond to a stimulus characteristic of a specific subcellular location. In this work, two rhodamine-peptides that form stable nanotubes at physiological pH but dissociate into highly fluorescent monomers within the acidified interior of endosomal/lysosomal cellular compartments have been developed. The rhodamine dipeptide conjugates, NH<sub>2</sub>-KK(RhB)-NH<sub>2</sub> (RhB-KK) and NH<sub>2</sub>-EK(RhB)-NH<sub>2</sub> (RhB-KE) with rhodamine B chromophores appended at the ε-amino position of a lysine residue, were shown to assemble into well-defined nanotubes at pH values above  $\sim$ 4–5 and to dissociate into a fluorescent monomer state at lower pH values. The pH dependence of the assembly process was investigated using circular dichroism (CD) and fluorescence spectroscopy along with transmission electron microscopy



(TEM), atomic force microscopy (AFM), and confocal imaging. Although the ring opening/closing transition of the rhodamine chromophore took place at pH 4.1 for both peptides, the onset of assembly began at pH 4.6 for RhB-KE and at a comparatively more basic pH (5.8) for RhB-KK. Accordingly, the rhodamine-peptides interconverted between three pH-dependent states: an open-ring, monomeric state ( $\lambda_{max}$  580 nm,  $\lambda_{ex}$  550 nm) at pH values at or below ~4.6; a closed-ring, nanotube form that exhibits AIEE ( $\lambda_{max}$  460 nm,  $\lambda_{ex}$  = 330 nm) at higher pH values; a closed-ring, nonemissive monomeric state that emerged below the critical micelle concentrations (CMC). The pH-responsive features of the peptides were evaluated by live-cell imaging in three cancer cell lines using confocal laser scanning microscopy (CLSM). Visualizing the cells after incubation with either RhB-KE or RhB-KK produced CLSM images with a punctate appearance in the Texas Red channel that colocalized with the lysosomes. These experiments indicate that the nanotubes were rapidly trafficked into the acidic lysosomal compartments within the cells, which induced dissociation into a monomeric, open state. Uptake inhibition studies suggested that cellular uptake was mediated by either caveolae- or clathrin-mediated endocytosis, depending on the cell line studied.

KEYWORDS: self-assembly, peptides, pH-responsivity, live-cell imaging, nanotubes

#### 1. INTRODUCTION

Nanotechnology offers a tremendous opportunity to facilitate the delivery of therapeutic agents and increase the efficacy of treatment. 1-3 The efficacy of these systems relies on the capability to control the rate and location of drug release, especially for antitumor drugs. 4,5 Nanoparticles often enter the cell via endocytosis, eventually becoming entrapped within endosomes and lysosomes.<sup>6,7</sup> Intracellular pH plays a critical role in the regulation of cellular growth<sup>8,9</sup> and proliferation<sup>10</sup> and tumor growth 11,12 and is distinct among various regions and organelles within the cell.<sup>13</sup> For example, although extracellular and cytosolic pH values are 7.2 and 7.4, respectively, the maturation of endosomes coincides with a progressive reduction in pH from the early (pH 6.3) to the late endosome (pH 5.5) and ultimately the lysosome (pH 4.7). Various strategies have been developed to facilitate the escape of the nanoparticles from the endosomal compartments into the cytosol prior to degradation. 6,14 One strategy employs a

pH-responsive material that undergoes a physical change at a particular pH value, which triggers drug release from the endosome. Accordingly, pH-sensitive drug carriers that respond to regional variations in cellular pH remain stable at physiological pH but structurally reorganize within the acidified interior of the endosomal compartment. Additionally, the lower pH of tumor tissue relative to healthy tissues allows for selective targeting of tumors. The design of self-assembling nanostructures that undergo a pH-dependent structural reorganization in different environments will be

Received: May 3, 2024 Revised: August 21, 2024 Accepted: August 21, 2024 Published: August 28, 2024





Figure 1. pH-Dependent ring opening/closing, emission, and assembly state of rhodamine B dipeptides, RhB-KE ( $R = CO_2H$ ) and RhB-KK ( $R = CH_2CH_2NH_3^+$ ).

important for the rational design of functional biomaterials for imaging, pH sensing, and drug delivery.

Fluorescence nanoparticles have become an important tool in the field of bioimaging to correlate imaging with therapeutic and surgical regimens. <sup>24,25</sup> Accurately detecting the distribution of nanomaterials within various cellular and physiological compartments with high spatiotemporal resolution is important to determine the site and time of drug release. 26 A variety of pH probes have been developed to image and map the pH distribution within living cells.<sup>27</sup> The high fluorescent quantum yield, sensitivity, photostability, and biocompatibility of rhodamine-based fluorescent imaging agents make them particularly suitable as intracellular imaging agents.<sup>28–32</sup> Rhodamine dyes undergo a pH-dependent interconversion between a closed spirolactam form and an open-ring xanthene state. Although the open-ring form emits strong fluorescence under acidic conditions, ring closure to the spirocyclic state at higher pH dramatically reduces emission. In this work, we report the design of peptide-rhodamine nanostructures that dissociate at low pH and self-report the assembly state<sup>33–36</sup> via a change in emission wavelength.<sup>37</sup> The rhodamine-peptide assembly interconverts between two distinct, fluorescent states: a fluorescent, open-ring, monomeric state ( $\lambda_{max}$  580 nm) at pH values below 4.6 and a fluorescent, spirolactam, assembled state ( $\lambda_{\text{max}}$  460 nm) at higher pH values.

#### 2. RESULTS AND DISCUSSION

**2.1. Peptide Design.** To create an assembly process that responded structurally and spectroscopically to pH variations, we designed two rhodamine-peptide conjugates, NH<sub>2</sub>-KK-(RhB)-NH<sub>2</sub> (RhB-KK) and NH<sub>2</sub>-EK(RhB)-NH<sub>2</sub> (RhB-KE) with rhodamine B chromophores appended at the  $\varepsilon$ -amino position of a lysine residue (Figure 1 and Scheme S1). The peptide structures were designed to display different pH-dependent surface charges based on the protonation state of a lysine or glutamate residue in the sequence (Figures S1–S3). For example, RhB-KE maintained a negative zeta ( $\zeta$ )-potential

above pH 4.2, whereas a positive  $\zeta$ -potential was recorded for RhB-KK over the entire pH range (Figure 5). The overall amphiphilicity of these peptides could be controlled by the pH-dependent state of the rhodamine B chromophore, which existed in a charged, fluorescent, ring-open state at low pH and in a nonpolar, nonfluorescent, spirocyclic state at high pH. As the peptide side chains of both sequences were charged, the presence of the protonated, open-state rhodamine chromophore of the opposite face of the sequence rendered the molecules highly hydrophilic. However, at high pH values, the peptide structures became amphiphilic due to the positioning of the hydrophobic, closed-form of rhodamine on the peptide face opposite that of the charged lysine/glutamate side chains. We reasoned that the alternating hydrophobic and polar sequence in this spirocyclic state would replicate the amphiphilic structure of  $\beta$ -sheet peptides<sup>25,38-41</sup> and induce self-assembly. At lower pH values, the ring opening to the charged state of the dye would diminish the peptide amphiphilicity, resulting in the dissociation of the assembled structure.

The pH-dependent interconversion between the ring-open (o) and ring-closed (c) forms of the rhodamine chromophore in both peptides was similar in water and PBS (Figures S4-S6). Both RhB-KE and RhB-KK exhibited absorptions at pH 3.6/3.7 (water, 0.25 mM) in the ultraviolet-visible (UV-vis) spectrum at ~560 nm and an emission peak at ~580 nm ( $\lambda_{\rm ex}$  = 550 nm), consistent with the presence of the open-ring form of the rhodamine chromophore. At pH 4.6, ring closure to the spirolactam form was accompanied by the loss of the emission peak at 580 nm along with the appearance of absorptions at 240 and 320 nm. Probing the emission of the open-ring state with increasing pH revealed a progressive decrease in emission, becoming completely quenched at pH 6.3/5.8 (RhB-KE/RhB-KK), similar to other reported rhodamine spirolactam derivatives.<sup>31</sup> The pH-dependent decrease in emission starting at pH  $\sim$  4.6 emerged from the progressive ring-closing reaction

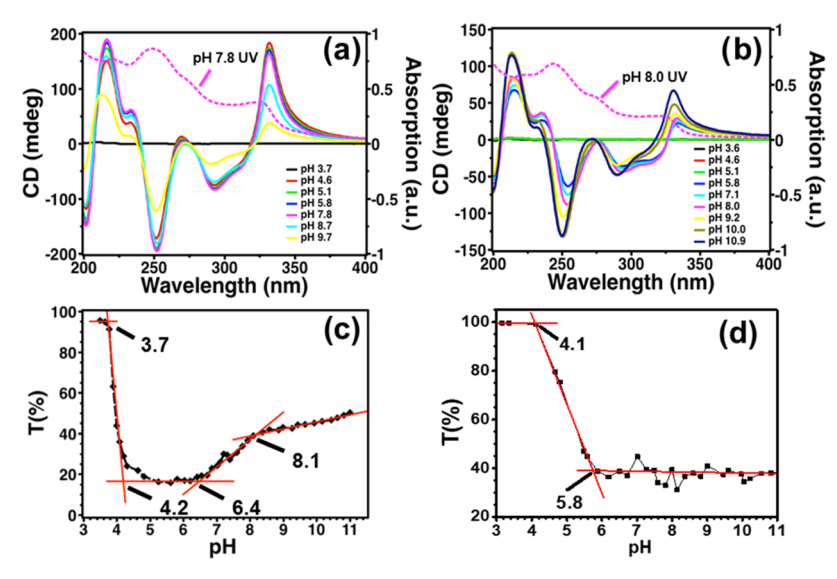


Figure 2. (a) CD spectra (0.25 mM, H<sub>2</sub>O) and transmittance at 400 nm (0.25 mM, PBS) of RhB-KE (a, c) and RhB-KK (b, d) as a function of pH. The pH of the samples was adjusted using aqueous NaOH (200 mM) and HCl (3.7 wt %) and then aged for 4 h at each pH value.

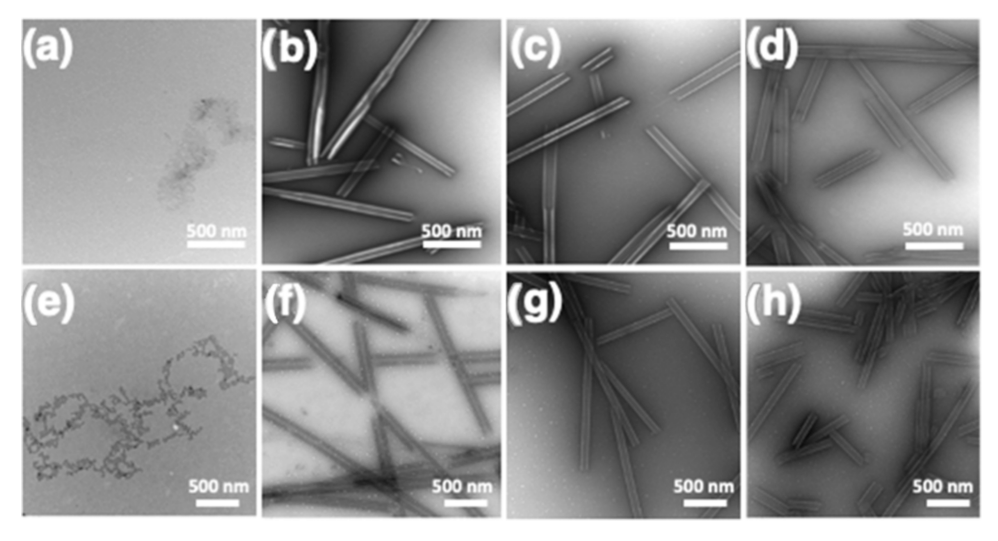


Figure 3. TEM images of RhB-KE and RhB-KK as functions of pH. RhB-KE at pH (a) 3.4, (b) 4.1, (c) 6.3, and (d) 8.8. RhB-KK at pH (e) 4.1, (f) 6.7, (g) 8.3, and (h) 9.0. Samples were prepared in water (1 mM) and aged for 12 h prior to imaging. TEM images were taken on copper-coated grids using uranyl acetate as a negative stain.

of the open, fluorescent state to the nonemissive spirolactam form.

Preliminary evidence for the pH dependence of the selfassembly process was apparent in the circular dichroic (CD) spectra in water (Figure 2a,b). Although the CD spectrum of RhB-KE was flat at pH 3.7 in water (0.25 mM), an apparent excitonic couplet, corresponding to a  $\pi$ - $\pi$  transition centered at 320 nm of the spirolactam form of the dye, appeared at pH 4.6 and remained constant over the range covering 4.6 to 9.7, at which point the couplet decreased in intensity. The appearance of CD signals in this pH range arose from the formation of aggregates stabilized by intermolecular  $\pi - \pi$ contacts, which facilitate propagation of the peptide backbone chirality to the rhodamine chromophore.<sup>42</sup> Lowering the pH from 9.7, above which the aggregate begins to dissociate, to 4.6 was accompanied by progressive red-shifting of the absorptions at 240 and 320 nm, consistent with J-type aggregation (Figure S4).<sup>43</sup> The pH dependence of the assembly of RhB-KK was similar to that of RhB-KE with two notable exceptions: (1)

although the ring opening/closing transition took place at pH 4.1, similar to RhB-KE, the onset of the assembly began at a comparatively more basic pH (5.8); (2) the extent of aggregation, as evidenced by CD, progressively increased as pH was increased from 5.8 to 11. The shape and pH dependence of the CD spectra of both peptides were qualitatively similar in PBS (Figure S5); however, the assembly process was more strongly driven in PBS than in water due to salt-mediated charge screening. He for example, in contrast to the flat signals observed at pH 3.7 in water, the spectral features of the assembly of both RhB-KE and RhB-KK were retained at a minimum intensity at this pH, even at a lower concentration in PBS (0.125 mM).

The aggregation of the peptides was further assessed by monitoring the transmittance at 400 nm in the UV spectra in PBS, a transparent spectral region for both the open and closed forms of the rhodamine dye (Figure 2c,d). As shown in Figure 2c, the aggregation of RhB-KE exhibited four distinct regions over the pH range from 3.7 to 11.0: (Region 1) pH 3.7–4.2,

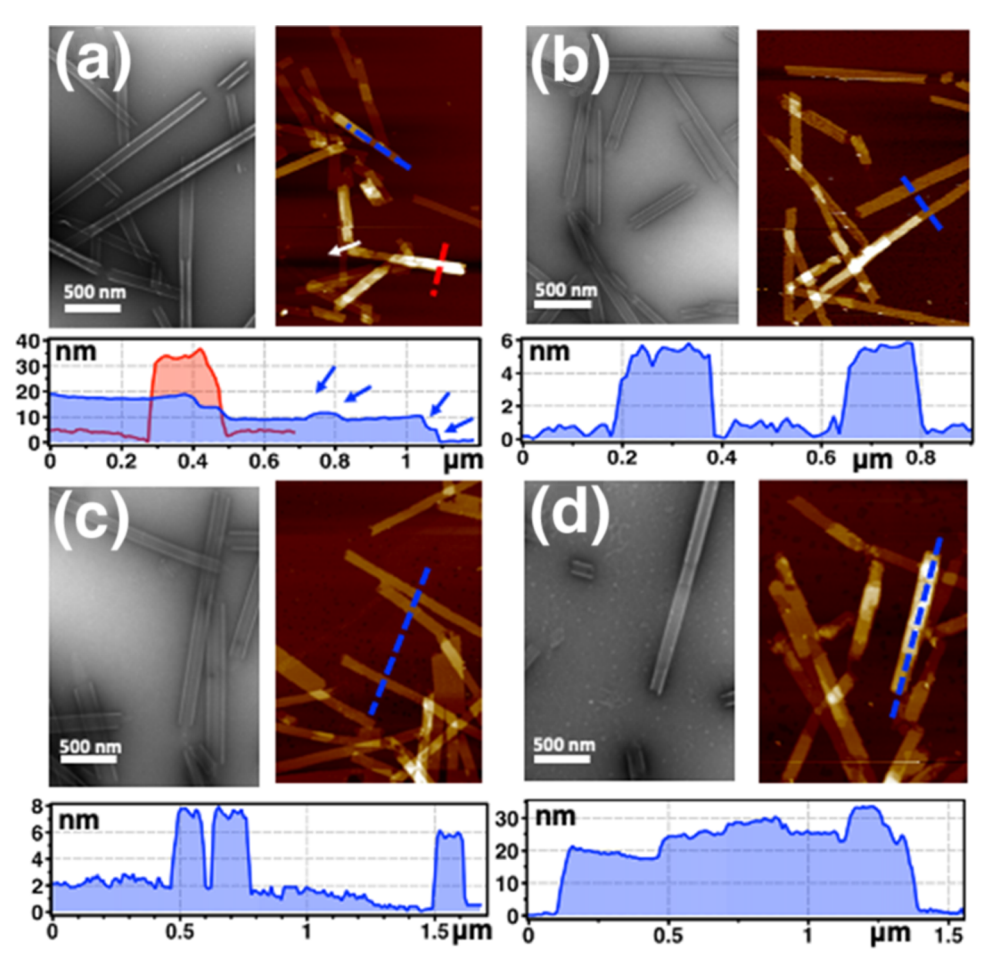


Figure 4. TEM and AFM images of RhB-KE at pH (a) 6.7 (b) 8.8 and RhB-KK at pH (c) 8.8 and (d) 10.5 in water at 1 mM, after aging for 12 h. TEM images were taken on copper-coated grids using uranyl acetate as a negative stain. AFM images were taken by drop-casting on a fresh cleaved

ring closing/opening; (Region 2) pH 4.2-6.4; (Region 3) pH 6.4-8.1; (Region 4) pH above 8.1. Initially at pH 3.7, the high transmittance (~97%), characteristic of a monomeric state of the peptide, abruptly decreased at pH 4.2, precisely coincident with the open-closed state transition of the rhodamine dye, as evidenced by the concomitant disappearance of the fluorescence (580 nm) of the open state and the emergence of a strong CD signal at this pH. The second region maintained a constant transmittance (~20%) between pH 4.2 and 6.4, indicating the emergence of an assembled state. Interestingly, the transmittance increased as the pH varied from 6.4 to 8.1 and then continued to increase at a lower rate between pH 8.1 and 11.0. As will become apparent in the following imaging studies, the change in transmittance occurring between pH 6.4 and 8.1 reflects alterations of the wall thickness of the assembled nanotubes, and changes in the pH range of 8.1 to 11.0 emerged from disassembly induced by intermolecular electrostatic repulsion. In contrast, the transmittance of RhB-KK rapidly decreased in the range of pH 4.1-5.8 and remained constant at higher pH values (Figure 2d), consistent with ring closure taking place at pH values above 4.1.

The self-assembly of both peptides was probed by transmission electron microscopy (TEM) and atomic force microscopy (AFM) as a function of the pH in water and PBS (Figure 3). Accordingly, TEM images of RhB-KE, recorded over a pH range of 3.4-10.2 in water, revealed the formation of well-defined nanotubes at all pH values except 3.4, where no

discernible structures were apparent, consistent with the light scattering and CD data indicating a monomeric state of the peptide at this pH (Figure 3a-d). A closer inspection of the TEM and AFM images showed that both the nanotube diameters and wall thicknesses decreased with increasing pH. For example, the diameters, measured by TEM, varied from  $114.2 \pm 15.4$  nm at pH 4.1 to  $97.5 \pm 9.1$  nm at pH 10.2, in conjunction with the wall thicknesses, measured by AFM, which decreased from  $30.5 \pm 13.3$  to  $7.7 \pm 1.9$  nm over the same range (Figures 4a,b, and S7). The structural changes that emerged during the pH transition from 6.4 to 8.1 (region 3) were particularly pronounced, corresponding to an abrupt increase in transmittance (Figure 2c). The AFM crosssectional heights at pH 8 (region 4) were ~6 nm, which were considerably smaller than the diameters measured by TEM, due to compression of the nanotube by the AFM tip. Thus, the cross-sectional heights of 6 nm reflected a wall thickness of ~3 nm, indicating a bilayer wall structure composed of two RhB-KE molecules with extended lengths of ~1.8 nm (Figure S13). Conversely, at the low end of the third pH range (pH 6.7), multiple cross-sectional heights were apparent (20 (blue) and 35 (red) nm, Figure 4a) due to the formation of multilayer wall structures among the nanotubes. Primarily multiwalled RhB-KE nanotubes were observed by AFM imaging in region 2 (pH 4.2-6.4) (Figure S7). It is noteworthy that at the higher end of the pH range (pH 8.0), single nanotubes with multiple cross-sectional heights that

change in  $\sim$ 5 nm steps could be observed by AFM, indicating the partial erosion of the multilayer structure at this pH (Figure S13). Thus, the pH-dependent assembly process was comprised of multiwalled (pH 4.1–6.4, region 2) and single-walled nanotubes (pH 8.1–10.2, region 4) separated by a transition range occurring between 6.4 and 8.1 (region 3), where both single- and multilayers wall thicknesses were present. In PBS (pH 7.4, 1 mM), RhB-KE was also assembled into well-defined nanotubes with diameters of 116  $\pm$  16 nm, similar to the dimensions observed in water (Figure S9). In contrast to RhB-KE, RhB-KK only exhibited nanotubes with multilayer wall thicknesses by AFM imaging above pH 8.8 in water (Figures 4c,d, and S8), at which point the positive  $\zeta$ -potential started to decrease (Figure 5). The diameters,

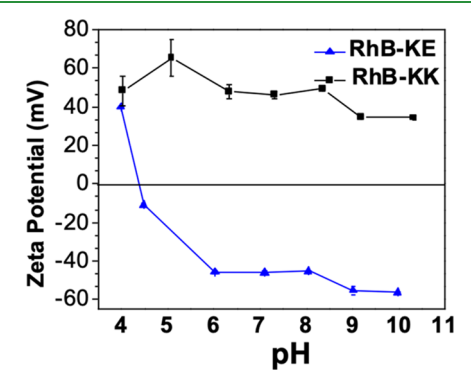


**Figure 5.** pH-Dependent  $\zeta$ -potentials of **RhB-KE** and **RhB-KK**. Samples were prepared in water (0.25 mM) and pH values were adjusted with aqueous HCl and NaOH. After 4 h,  $\zeta$ -potential measurements were recorded.

measured by TEM, varied slightly from 89.9  $\pm$  9.5 nm at pH 9.0 to 96.9  $\pm$  12.6 nm at pH 10.5 while the wall thicknesses increased from 6.7  $\pm$  0.7 to 16.0  $\pm$  3.5 nm. The AFM cross-sectional heights at pH 8.8 were ~6 nm, while at pH 10.5, multiple cross-sectional heights from ~20 to ~34 nm were present, reflecting the formation of multiwalled nanotubes (Figure 4c,d). In PBS (pH 7.4, 1 mM), the assembly of RhB-KK produced an array of nanofibers after 4 h but subsequently progressed over the next 8 h to nanotubes with slightly smaller diameters (diameters: 79  $\pm$  3.6 nm), compared with the nanotubes formed in pure water (Figures S10 and S12). The pH dependence of the assembly of RhB-KE and RhB-KK was similar in water and PBS (Figures 3 and S11–S12).

The base titration curves of RhB-KE and RhB-KK, coupled with zeta ( $\zeta$ ) potential measurements, provided insight into the differing pH-dependent assembly profiles and the formation of multiwalled nanotubes (Figures 5, and S2-S3). RhB-KE exhibited an isoelectric pH (pI) of 4.2, displaying a more negative  $\zeta$ -potential as the pH was increased. The occurrence of the pI at 4.2 coincided with the onset of the transition of the protonated, open-ring form of the rhodamine chromophore to the neutral spirolactam state, which induced a progressive change in  $\zeta$ -potential from positive to negative as the pH was increased. Accordingly, the onset of self-assembly of RhB-KE at 4.2 coincided with the pI due to the presence of minimal intermolecular electrostatic repulsion in this region. As shown in Figure 5, the  $\zeta$ -potential becomes increasingly more negative as the pH increases from ~4.1 to 6.4. Thus, in the lower region of this pH range (Figure 2c, region 2), a lower surface potential permitted the growth of larger nanotubes comprised of

multilayer walls. The stability of nanoscale colloidal structures, such as nanotubes, is determined by the balance of repulsive and attractive van der Waals forces between the nanoparticles, as described by DLVO theory. 45 Higher surface charge on the nanotubes favors a dispersion of smaller nanotubes because repulsive electrostatic interactions kinetically hamper the formation of larger, thermodynamically more favorable particles. When the surface charge was low, as in the pH range of region 2 near the pI of RhB-KE, attractive van der Waals forces favored the assembly of larger, multilayer wall structures. 46,47 At higher pH values, the greater negative surface charge gradually attenuated the assembly process and led to smaller diameter nanotubes. Accordingly, as the pH varied from 6.4 to 8.0, the ratio of multi- to single-walled nanotubes progressively decreased as the surface charge became slightly more negative over this pH range. In contrast, RhB-KK displayed positive ζ-potentials over the entire pH range, which became less positive at pH values above 8.1. Thus, the assembly process commenced for RhB-KK at a slightly higher pH value of 5.8, compared with RhB-KE, and became increasingly efficient at higher pH values, forming nanotubes with multilayer walls at pH values above 8.8. The increase in wall thickness going from pH 8.8 to 10.5 emerged from the corresponding decrease in  $\zeta$ -potential, which induces the formation of a multilayer nanotube wall. The hydrodynamic diameters were measured to be 786 nm (Z-avg., PDI 0.23) and 690 nm (Z-avg., PDI 0.28) for RhB-KE and RhB-KK, respectively, in water at pH 7.4. Deconvolution of the FT-IR spectra of the RhB-KE and RhB-KK nanotubes at pH 8.1 indicated that the wall structures of the RhB-KE and RhB-KK nanotubes contained  $\sim$ 65 and  $\sim$ 81%  $\beta$ -sheet character, respectively (Figure S14).

The fluorescence of the rhodamine chromophore could be exploited to report information about the assembly state of the nanotubes and the pH of the local environment. For example, the appearance of a strong rhodamine emission at 580 nm ( $\lambda_{ex}$ = 550 nm) indicated the dissociation of the RhB-KE and RhB-KK nanotubes into monomers at low pH values, which was induced by the ring opening of the rhodamine spirolactam in an acidic environment (Figure S6). Although the spirolactam forms were colorless and not emissive in the monomeric state, as expected for rhodamine dyes, self-assembly of the closedring state of both peptides into the nanotubes stimulated emission at 450-460 nm ( $\lambda_{ex}$  330 nm) in PBS (pH 7.4), characteristic of aggregation-induced emission enhancement (AIEE) (Figure S15).<sup>48,49</sup> The critical micelle concentrations (CMC) of RhB-KE and RhB-KK were determined to be 18 and 52  $\mu$ M, respectively, using pyrene as a fluorescent probe (Figure S16). 50,51 To confirm that AIEE was the source of emission at 450-460 nm, the fluorescence intensity was recorded over a concentration range of 1-250 µM in PBS, which showed an approximately linear increase in intensity with concentration (Figure S17). Emission emerged at ~10 and 25 µM in PBS for RhB-KE and RhB-KK, respectively, corresponding to the CMC values. To confirm the occurrence of aggregation-induced emission, the emission was recorded as a function of increasing amounts of 2,2,2-trifluoroethanol (TFE) in PBS, which induced progressive dissociation of the nanotube into a monomer state (Figure 6). Conversion into a monomeric state with the addition of TFE was induced at 15-20% for RhB-KE and 0-5% TFE for RhB-KK in PBS, as indicated by the loss of a CD signal characteristic of the assembled states. Similarly, the emission at 450-460 nm

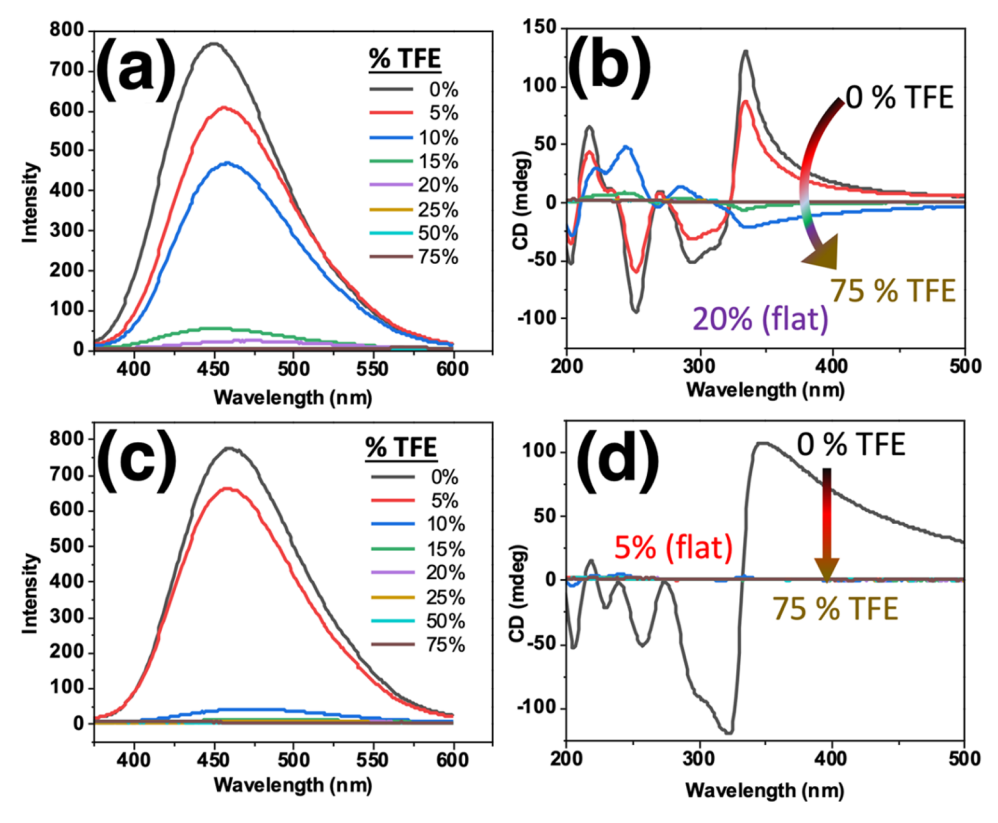


Figure 6. Aggregation-induced emission enhancement ( $\lambda_{em}$  = 460 nm,  $\lambda_{ex}$  = 330 nm) and CD spectra of (a, b) RhB-KE and (c, d) RhB-KK as a function of the amount of TFE in PBS. Samples of each peptide were aged at 0.125 and 0.25 mM in TFE/PBS for the emission and CD spectra, respectively.

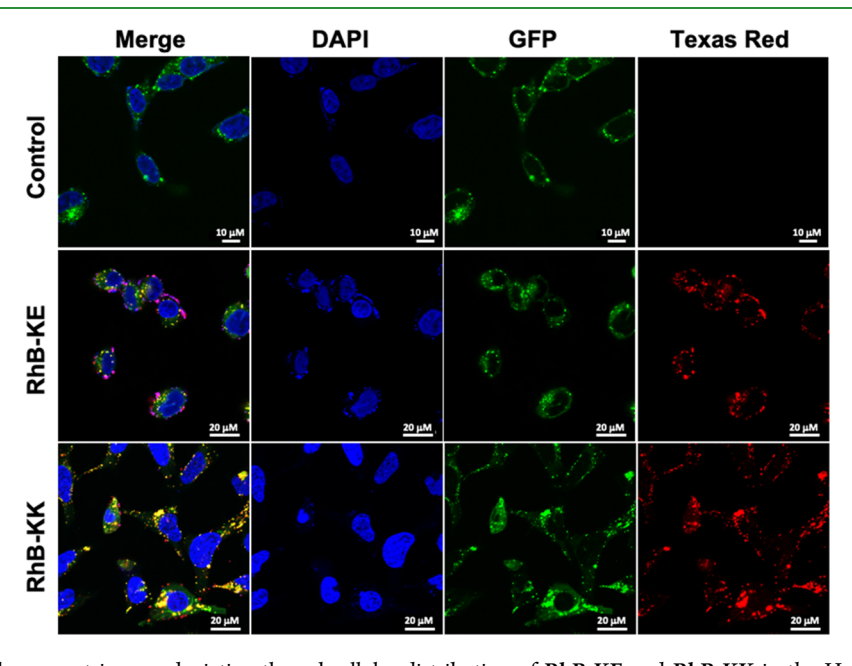


Figure 7. Confocal laser fluorescent images depicting the subcellular distribution of RhB-KE and RhB-KK in the HepG2 cell line. HepG2 cells were incubated with RhB-KE (0.1 mM, 16 h) and RhB-KK (0.1 mM, 4.5 h) and costained with LysoTracker green DND-26 (lysosome stain) and Hoechst 33258 (nuclear stain) and compared to a control without any added peptides. Cells were visualized in the DAPI ( $\lambda_{exc}$ . 402 nm,  $\lambda_{em}$ . 425–475 nm), GFP ( $\lambda_{exc}$ . 487 nm,  $\lambda_{em}$ . 500–550 nm), and Texas Red ( $\lambda_{exc}$ . 561 nm,  $\lambda_{em}$ . 570–620 nm) and then overlaid in the merged channel.

vanished at similar points in the titration with TFE, consistent with aggregation-enhanced fluorescence.

Nanoparticles usually enter cells via endocytosis, which enclose them in endosomal compartments that ultimately traffic them to the lysosomes for degradation. <sup>52</sup> The ability of

the peptide nanotubes to respond to subcellular pH variations and self-report their assembly state via fluorescence was evaluated by live-cell imaging in HepG2 human liver cancer cells using confocal laser scanning microscopy (CLSM). <sup>53</sup> The cells were incubated with the peptides and labeled with

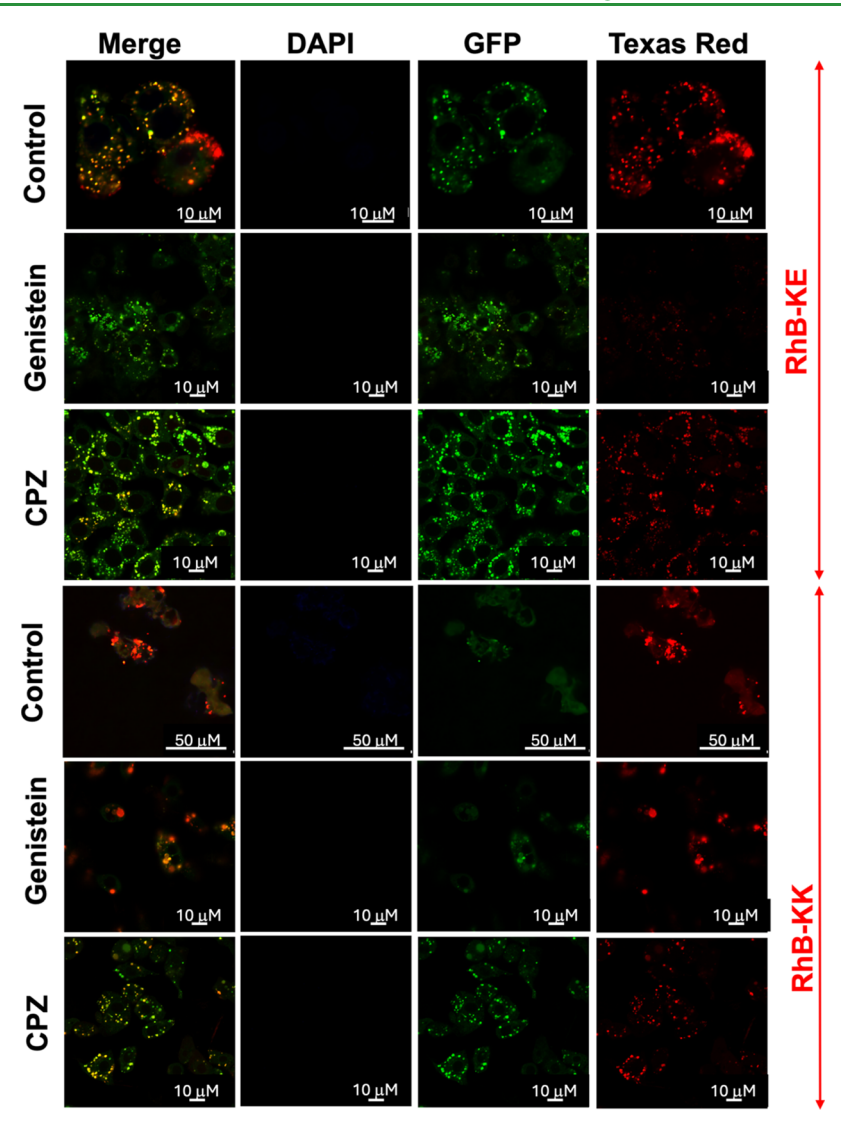


Figure 8. Confocal laser fluorescent images showing the impact of endocytosis inhibitors genistein and chlorpromazine (CPZ) on the uptake of RhB-KE and RhB-KK into the HepG2 cell line. HepG2 cells were separately treated with 10 μM CPZ and 100 μM genistein. After 1 h, the medium was discarded, and cells were washed with PBS. Cells were then incubated with RhB-KE (0.1 mM) or RhB-KK (0.1 mM). After 1 h, the cells were washed with PBS and incubated with LysoTracker green DND-26 for 1 h before imaging. Cells were visualized in the DAPI ( $\lambda_{\rm exc}$ . 402 nm,  $\lambda_{\rm em.}$  425–475 nm), GFP ( $\lambda_{\rm exc}$ . 487 nm,  $\lambda_{\rm em.}$  500–550 nm), and Texas Red ( $\lambda_{\rm exc}$ . 561 nm,  $\lambda_{\rm em.}$  570–620 nm), then overlaid in the merged channel, and compared to a control without any added inhibitors.

Hoechst 33258 and LysoTracker Green DND-26 to indicate the location of the nucleus and lysosomes, respectively, and imaged over 24 h by CLSM (Figures S19-S20). Although the confocal system was capable of excitation only at wavelengths at or higher than 402 nm, samples containing only RhB-KE and RhB-KK nanotubes at pH 7.4 (PBS) could be partially visualized in the DAPI channel ( $\lambda_{\rm exc}$ . 402 nm). However, the inability to specifically excite the sample at 330 nm to induce AIEE emission at 460 nm hampered visualization of the intact nanotube in the images (Figure S18). The monomeric, open state of the peptides at low pH could be imaged by excitation in the Texas Red ( $\lambda_{\rm exc}$ . 561 nm) channel due to emission at ~580 nm. Accordingly, imaging the cells after incubation with either RhB-KE (0.1 mM, 16 h) or RhB-KK (0.1 mM, 4.5 h) produced images in the Texas Red channel with a punctate appearance typical of compounds encapsulated in vesicular membranes inaccessible to the cytoplasm (Figure 7).7 The punctate image in the Texas Red channel colocalized with the stained lysosomes when the channels were overlaid, with

Pearson's correlation coefficients of 0.98 for RhB-KK and 0.91 for RhB-KE after 24 h (Figures S21-S22), indicating that the peptides were trafficked into the acidic lysosomal compartments, which induced dissociation into a monomeric, open state. The lack of intact nanotubes within cells visualized in the DAPI channel, even after 1 h, suggested that upon uptake into the cells the peptides experienced rapid sequestration and disassembly within the endosomal compartments. To avoid overlap of the Hoechst 33258 stain with the weak emission of the nanotubes in the DAPI channel, the cells were incubated with high concentrations of RhB-KK (500  $\mu$ M) for 10 min, using only LysoTracker Green DND-26 to stain the lysosomes. Confocal imaging revealed a few intact nanotubes outside the cells in the bright-field and DAPI channels, along with red punctate emission in the Texas red channel. However, no intracellular nanotubes were visible (Figure S23), consistent with rapid uptake and dissociation within the lysosomes. It is noteworthy that the punctate emission in the Texas Red channel appeared more rapidly for RhB-KK than for RhB-KE,

likely due to the faster uptake of the positively charged RhB-KK nanotubes.5

We further explored the impact of endocytosis inhibitors on the uptake efficacy of the peptides to provide preliminary insight into the uptake mechanism of the peptides. Accordingly, HepG2 cells were separately incubated with genistein and chlorpromazine (CPZ) to inhibit caveolae- and clathrin-mediated endocytosis, respectively. 55,56 To reduce cytotoxicity, the cells were incubated with the inhibitors for only 1 h and then imaged by CLSM. As shown in Figure 8, the appearance of the punctate red emission in the Texas Red channel, indicative of uptake into the lysosomes, was significantly attenuated in the cells treated with genistein for both RhB-KE and RhB-KK, suggesting that caveolae-mediated endocytosis served as the primary uptake pathway. Further studies in PANC-1 pancreatic cancer cells showed that the uptake of both peptides was significantly reduced by both inhibitors after treatment for 1 h, compared with a control lacking the inhibitors, indicating the importance of both caveolae- and clathrin-mediated pathways for these cells (Figures S24-S25). Although genistein inhibited the viability of HT-29 colon cancer cells, as reported in prior studies, incubation with CPZ for 1 h prior to imaging also decreased the uptake of peptides (Figure S26). These studies confirmed that peptide uptake occurred by endocytosis via either or both caveolae- and clathrin-mediated pathways, depending on the cell line

#### 3. CONCLUSIONS

In summary, we have described a series of rhodamine-peptide nanotubes that respond to intracellular variations in pH and self-report their assembly state via an emission wavelength. The nanotubes transition between a fluorescent, monomeric state ( $\lambda_{max}$  580 nm) at low pH values and spirolactam, assembled state exhibiting AIEE ( $\lambda_{max}$  460 nm) at higher pH values. Accordingly, the peptides assembled into stable nanotubes at physiological pH (7.4) but rapidly dissociated in acidic environments due to the ring opening of the rhodamine chromophore. The capability of the peptides to structurally respond within the acidified interior of the lysosomal compartments of liver cancer cells was demonstrated by using confocal microscopy. We envisage this system to have potential utility in drug delivery vehicles whereby the pH variation of separate organs, tissues, or subcellular compartments, as well as their associated pathophysiological states, 12 could be exploited to induce disassembly and drug release.

## 4. EXPERIMENTAL SECTION

4.1. General Methods. Fluorescence microscopy experiments were performed on a Nikon A1R Live Cell Confocal microscope equipped with a 32-channel PMT spectral detector. Transmission electron microscopy (TEM) was conducted with a Technai G2 Spirit instrument running at 80.0 kV. Fluorescence excitation and emission experiments were performed on a Shimadzu RF-5301PC Spectrofluorometer. Circular dichroism (CD) measurements were run with a JASCO J-815 CD Spectrometer at 23 °C. All UV measurements were conducted using a Shimadzu UV-2450 spectrophotometer in a 3 mm path length quartz cuvette at 23 °C. The pH measurements were obtained using a Mettler Toledo MP 125 pH meter with an InLab Micro pH probe. ESI mass spectra were recorded on a Bruker MicrOTOF. ζ-Potentials were measured on a Malvern Zetasizer NanoZS system with irradiation from a 632.8 nm He-Ne laser. Nikon A1R Live Cell Confocal instrument was used for the confocal

experiments. <sup>1</sup>H and <sup>13</sup>C NMR were recorded at either 400 or 600 MHz on a Bruker Advance III instrument.

- 4.2. General Peptide Preparation. The protected dipeptides were manually prepared using Fmoc/t-Bu solid-phase peptide synthesis on rink amide resin (loading of 0.74 mmol/g). Protected amino acids were coupled by standard techniques: Fmoc-amino acid, 2-(1H-benzotriazol-1-yl)-1,1,3,3-tetramethyluronium hexafluorophosphate (HBTU), 1-hydroxybenzotriazole (HOBt) (300 mol % each relative to resin), and N,N-diisopropylethylamine (DIPEA) (600 mol % relative to resin) coupled in DMF for 12 h. Piperidine (20% in DMF) was used for Fmoc deprotection. 2% TFA with 2% TES in DCM was used to deprotect the Mtt group. The rhodamine peptides were cleaved from the resin with TFA/water/triethylsilane (95:1:4) at room temperature for 2 h. The crude peptides were precipitated with cold diethyl ether and purified by reversed-phase HPLC on a preparative Varian Dynamax C18 column eluting with a linear gradient of acetonitrile/water containing 0.1% TFA (10:90 to 100:0 over 30 min) and stored as lyophilized powders at 0 °C. Peptide purity was assessed by analytical reverse-phase HPLC, and identity was confirmed using ESI-TOF mass spectrometry and NMR. RhB-KK: <sup>1</sup>H NMR (400 MHz, DMSO-d6)  $\delta$  8.34 (1H, d, J = 7.8 Hz), 8.10-8.00 (3H, m), 7.80-7.73 (1H, m), 7.71-7.61 (2H, m), 7.54-7.43 (2H, m), 7.42-7.38 (1H, s), 7.06-7.00 (1H, m), 7.00-6.97 (1H, s), 6.41-6.27 (6H, m), 4.19-4.05 (1H, m), 3.37-3.27 (8H, q, J = 6.9 Hz), 3.07-2.85 (2H, m), 2.77-2.65 (2H, m), 1.55-1.45 (2H, m), 1.43-1.25 (4H, m), 1.11-1.05 (12H, t, J = 7.0 Hz), and 1.04-0.98 (2H, m);  $^{13}$ C NMR (600 MHz, DMSO-d6)  $\delta$  173.02, 168.22, 166.87, 158.28, 158.08, 153.36, 152.63, 152.56, 148.22, 132.69, 130.47, 128.42, 128.34, 128.31, 123.63, 122.22, 108.33, 97.41, 63.98, 52.67, 51.80, 43.83, 38.49, 31.65, 30.43, 27.66, 26.43, 23.05, 20.88, and 12.34; [M]+ is 698.4383, calcd mass 698.4388. RhB-KE: <sup>1</sup>H NMR (400 MHz, DMSO- $d_6$ )  $\delta$  8.34 (1H, d, J = 7.8 Hz), 8.10–8.00 (3H, m), 7.80–7.73 (1H, m), 7.71–7.61 (2H, m), 7.38–7.33 (1H, s), 7.06-7.00 (1H, m), 7.00-6.97 (1H, s), 6.41-6.27 (6H, m), 4.19-4.05 (1H, m), 3.88-3.76 (2H, q, J = 5.4 Hz), 3.37-3.27 (8H, q, J = 5.4 Hz)7.0 Hz), 3.07-2.85 (2H, m), 2.39-2.30 (2H, m), 1.45-1.25 (2H, m), 1.12-1.05 (12H, t, J = 7.0 Hz), and 1.04-0.98 (2H, m);  $^{13}$ C NMR (600 MHz, DMSO- $d_6$ )  $\delta$  173.46, 172.88, 167.94, 166.86, 158.20, 158.00, 153.36, 152.63, 152.56, 148.27, 132.68, 130.50, 128.43, 128.34, 128.31, 123.63, 122.23, 108.33, 97.40, 63.99, 52.78, 51.42, 43.81, 31.59, 28.95, 27.67, 26.48, 23.08, and 12.36; [M]<sup>+</sup> is 699.3864, calcd mass 699.3865.
- 4.3. Transmission Electron Microscopy. Samples were dropped on carbon-coated copper grids (Ted Pella, Inc.) for 2 min. After the removal of excess solution, the sample grid was negatively stained with 2% (w/w) uranyl acetate solution for 1 min. The dried specimen was observed with a Technai G2 Spirit TEM instrument operating at 80 keV. Images were analyzed with either FIJI or ImageJ imaging software.
- 4.4. Atomic Force Microscopy. AFM images were collected on the Bruker AXS Dimension Icon Atomic Force Microscope in ScanAsyst mode using Bruker AFM silicon tips with a nitride lever under a nitrogen atmosphere. The sample being analyzed was dropped on a freshly cleaved mica surface and dried before imaging with a resolution of 512 pixels × 512 pixels. AFM images were analyzed with Bruker NanoScope Analysis software.
- **4.5. Cell Culture.** Live-cell imaging was performed on the human liver cancer (Hep-G2) cell lines obtained from the American Type Culture Collection (ATCC, Manassas, GA). HepG2 cells were cultured in DMEM media supplemented with 10% FBS and 1% penicillin-streptomycin in an incubator at 37 °C and 5% CO<sub>2</sub>. Cells were subcultured every 2-3 days using 0.25% Trypsin-EDTA solution. The HepG2 cell line was purchased from ATCC (American Type Culture Center). DMEM media, FBS, PBS, 0.25% Trypsin-EDTA solution, penicillin-streptomycin, and Hoechst 33258 (Nucleus stain) were all purchased from Sigma-Aldrich. Tissueculture flasks and 35 mm (no. 1.5 coverslip) confocal dishes have been purchased from VWR International. Phenol red-free DMEM media and LysoTracker Green DND-26 have been purchased from ThermoFisher.

4.6. Confocal Laser Scanning Microscopy, Live-Cell imaging. Imaging was performed using a Nikon A1R Live Cell Confocal. Cells were seeded in a 35 mm (No. 1.5 coverslip) confocal dish and were allowed to adhere overnight (~12 h). Cell culture media were then discarded, and cells were washed with PBS (×3). Self-assembled (1 mM, PBS) RhB-KK and RhB-KE probes were then added to the cells with fresh culture media to get the final concentration of 100  $\mu$ M. Cells were then allowed to incubate at 37 °C and 5% CO<sub>2</sub> for the following incubation periods (in different confocal dishes): 1, 4.5, 16, and 24 h. After the respective incubation periods, cell media were discarded, and cells were washed with PBS (x3). Cells were then incubated for 1 h with LysoTracker green DND-26 (50 nM) dissolved in cell culture media for live-cell imaging. Hoechst 33258 (4  $\mu$ L) at a working concentration of 10  $\mu$ g/mL was also added before the incubation. Cells were washed three times with PBS. Cells were incubated only with LysoTracker green DND-26 and Hoechst 33258 for 1 h to serve as a control in this experiment. Live-cell imaging was then performed in Phenol-Red free DMEM media containing 1% penicillin-streptomycin using a Nikon A1R Live Cell Imaging Confocal Microscope using excitation lasers at 402, 487, and 561 nm.

4.6.1. Cellular Uptake Študies. HepG2, HT-29, and PANC-1 cells were all cultured separately in DMEM medium supplemented with 10% FBS and 1% penicillin–streptomycin. They were seeded in a 35 mm (No. 1.5 coverslip) confocal dish confocal dish and were allowed to adhere overnight. Cell media were then discarded, and cells were washed with PBS. Cells were then given a treatment of either (10  $\mu$ M CPZ and/or 100  $\mu$ M genistein) for 1 h. Cells were again washed with PBS and incubated with 100  $\mu$ M RhB-KK or RhB-KE and LysoTracker green DND-26 for 1 h. Cells were washed thrice with PBS and were imaged in Phenol-Red free DMEM media using a Nikon A1R live-cell microscope.

#### ASSOCIATED CONTENT

#### Supporting Information

The Supporting Information is available free of charge at https://pubs.acs.org/doi/10.1021/acsami.4c07280.

Experimental section; pka determination; pH-dependent  $\zeta$ -potentials; CMC measurements; CD, UV, fluorescence, and infrared spectra; TEM, AFM, and live-cell confocal imaging of rhodamine-peptides (PDF)

### AUTHOR INFORMATION

### **Corresponding Author**

Jon R. Parquette – Department of Chemistry and Biochemistry, The Ohio State University, Columbus, Ohio 43210, United States; orcid.org/0000-0002-4803-028X; Email: Parquette.1@osu.edu

### **Authors**

Ziyuan Meng — Department of Chemistry and Biochemistry, The Ohio State University, Columbus, Ohio 43210, United States

Sagarika Taneja – Department of Chemistry and Biochemistry, The Ohio State University, Columbus, Ohio 43210, United States

Reham Hassan – Department of Chemistry and Biochemistry, The Ohio State University, Columbus, Ohio 43210, United States

Complete contact information is available at: https://pubs.acs.org/10.1021/acsami.4c07280

#### **Author Contributions**

<sup>†</sup>Z.M. and S.T. contributed equally to this work. The manuscript was written through the contributions of all

authors. All authors have given their approval to the final version of the manuscript.

#### Notes

The authors declare no competing financial interest.

### ACKNOWLEDGMENTS

This material is based upon work supported by the National Science Foundation (CHE-2106924). Electron microscopy was performed at the Center for Electron Microscopy and Analysis (CEMAS) at The Ohio State University. We also acknowledge resources from the Campus Microscopy and Imaging Facility (CMIF) and the OSU Comprehensive Cancer Center (OSUCCC) Microscopy Shared Resource (MSR), The Ohio State University. This facility is supported in part by grant P30 CA016058, National Cancer Institute, Bethesda, MD.

#### **■** REFERENCES

- (1) Liu, J.; Zhang, R.; Xu, Z. P. Nanoparticle-Based Nanomedicines to Promote Cancer Immunotherapy: Recent Advances and Future Directions. *Small* **2019**, *15*, No. 1900262.
- (2) Williams, R. M.; Chen, S.; Langenbacher, R. E.; Galassi, T. V.; Harvey, J. D.; Jena, P. V.; Budhathoki-Uprety, J.; Luo, M.; Heller, D. A. Harnessing nanotechnology to expand the toolbox of chemical biology. *Nat. Chem. Biol.* **2021**, *17* (2), 129–137.
- (3) Meng, Y.; Han, S.; Yin, J.; Wu, J. Therapeutic Copolymer from Salicylic Acid and l-Phenylalanine as a Nanosized Drug Carrier for Orthotopic Breast Cancer with Lung Metastasis. ACS Appl. Mater. Interfaces 2023, 15 (35), 41743–41754.
- (4) Kanamala, M.; Wilson, W. R.; Yang, M.; Palmer, B. D.; Wu, Z. Mechanisms and biomaterials in pH-responsive tumour targeted drug delivery: A review. *Biomaterials* **2016**, 85, 152–167.
- (5) Zhou, S.; Shang, Q.; Wang, N.; Li, Q.; Song, A.; Luan, Y. Rational design of a minimalist nanoplatform to maximize immunotherapeutic efficacy: Four birds with one stone. *J. Controlled Release* **2020**, 328, 617–630.
- (6) Patel, S.; Kim, J.; Herrera, M.; Mukherjee, A.; Kabanov, A. V.; Sahay, G. Brief update on endocytosis of nanomedicines. *Adv. Drug Delivery Rev.* **2019**, *144*, 90–111.
- (7) Selby, L. I.; Cortez-Jugo, C. M.; Such, G. K.; Johnston, A. P. R. Nanoescapology: progress toward understanding the endosomal escape of polymeric nanoparticles. *WIREs Nanomed. Nanobiotechnol.* **2017**, 9 (5), No. e1452.
- (8) Martínez-Zaguilán, R.; Chinnock, B. F.; Wald-Hopkins, S.; Bernas, M.; Way, D.; Weinand, M.; Witte, M. H.; Gillies, R. J. [Ca2+]i and pH in omeostasis in Kaposi Sarcoma cells. *Cell. Physiol. Biochem.* **1996**, *6* (3), 169–184.
- (9) Humez, S.; Monet, M.; van Coppenolle, F.; Delcourt, P.; Prevarskaya, N. The role of intracellular pH in cell growth arrest induced by ATP. *Am. J. Physiol.: Cell Physiol.* **2004**, 287 (6), C1733—C1746.
- (10) Czepán, M.; Rakonczay, Z.; Varró, A.; Steele, I.; Dimaline, R.; Lertkowit, N.; Lonovics, J.; Schnúr, A.; Biczó, G.; Geisz, A.; et al. NHE1 activity contributes to migration and is necessary for proliferation of human gastric myofibroblasts. *Pflugers Arch. Eur. J. Physiol.* **2012**, 463 (3), 459–475.
- (11) Schindler, M.; Grabski, S.; Hoff, E.; Simon, S. M. Defective pH regulation of acidic compartments in human breast cancer cells (MCF-7) is normalized in adriamycin-resistant cells (MCF-7adr). *Biochemistry* **1996**, *35* (9), 2811–2817.
- (12) Webb, B. A.; Chimenti, M.; Jacobson, M. P.; Barber, D. L. Dysregulated pH: a perfect storm for cancer progression. *Nat. Rev. Cancer* 2011, 11 (9), 671–677.
- (13) Casey, J. R.; Grinstein, S.; Orlowski, J. Sensors and regulators of intracellular pH. *Nat. Rev. Mol. Cell Biol.* **2010**, *11* (1), 50–61.

- (14) Yameen, B.; Choi, W. I.; Vilos, C.; Swami, A.; Shi, J.; Farokhzad, O. C. Insight into nanoparticle cellular uptake and intracellular targeting. *J. Controlled Release* **2014**, *190*, 485–499.
- (15) Bazban-Shotorbani, S.; Hasani-Sadrabadi, M. M.; Karkhaneh, A.; Serpooshan, V.; Jacob, K. I.; Moshaverinia, A.; Mahmoudi, M. Revisiting structure-property relationship of pH-responsive polymers for drug delivery applications. *J. Controlled Release* **2017**, 253, 46–63.
- (16) Hussain, M. S.; Khetan, R.; Clulow, A. J.; Ganesan, R.; MacMillan, A.; Robinson, N.; Ahmed-Cox, A.; Krasowska, M.; Albrecht, H.; Blencowe, A. Teaching an Old Dog New Tricks: A Global Approach to Enhancing the Cytotoxicity of Drug-Loaded, Non-responsive Micelles Using Oligoelectrolytes. ACS Appl. Mater. Interfaces 2024, 16 (8), 9736–9748.
- (17) Cheng, R.; Meng, F.; Deng, C.; Klok, H.-A.; Zhong, Z. Dual and multi-stimuli responsive polymeric nanoparticles for programmed site-specific drug delivery. *Biomaterials* **2013**, *34* (14), 3647–3657.
- (18) Pang, X.; Jiang, Y.; Xiao, Q.; Leung, A. W.; Hua, H.; Xu, C. pH-responsive polymer—drug conjugates: Design and progress. *J. Controlled Release* **2016**, 222, 116–129.
- (19) Mano, J. F. Stimuli-responsive polymeric systems for biomedical applications. *Adv. Eng. Mater.* **2008**, *10* (6), 515–527.
- (20) Liu, L.; Fu, L.; Jing, T.; Ruan, Z.; Yan, L. pH-Triggered Polypeptides Nanoparticles for Efficient BODIPY Imaging-Guided Near Infrared Photodynamic Therapy. ACS Appl. Mater. Interfaces 2016, 8 (14), 8980–8990.
- (21) Liu, Z.; Hao, X.; Qian, J.; Zhang, H.; Bao, H.; Yang, Q.; Gu, W.; Huang, X.; Zhang, Y. Enzyme/pH Dual-Responsive Engineered Nanoparticles for Improved Tumor Immuno-Chemotherapy. ACS Appl. Mater. Interfaces 2024, 16 (10), 12951–12964.
- (22) Gerweck, L. E.; Seetharaman, K. Cellular pH gradient in tumor versus normal tissue: Potential exploitation for the treatment of cancer. *Cancer Res.* **1996**, *56* (6), 1194–1198.
- (23) Izumi, H.; Torigoe, T.; Ishiguchi, H.; Uramoto, H.; Yoshida, Y.; Tanabe, M.; Ise, T.; Murakami, T.; Yoshida, T.; Nomoto, M.; Kohno, K. Cellular pH regulators: potentially promising molecular targets for cancer chemotherapy. *Cancer Treat. Rev.* **2003**, *29* (6), 541–549.
- (24) Yang, Z.; Usama, S. M.; Li, F.; Burgess, K.; Li, Z. A zwitterionic near-infrared dye linked TrkC targeting agent for imaging metastatic breast cancer. *MedChemComm* **2018**, 9 (10), 1754–1760.
- (25) Park, J. Y.; Kim, J.; Ha, J. S.; Kim, Y. Self-Assembled Tamoxifen-Selective Fluorescent Nanomaterials Driven by Molecular Structural Similarity. *ACS Appl. Mater. Interfaces* **2024**, *16* (5), 5462–5473.
- (26) Hou, J.-T.; Ren, W. X.; Li, K.; Seo, J.; Sharma, A.; Yu, X.-Q.; Kim, J. S. Fluorescent bioimaging of pH: from design to applications. *Chem. Soc. Rev.* **2017**, *46* (8), 2076–2090.
- (27) Yue, Y.; Huo, F.; Lee, S.; Yin, C.; Yoon, J. A review: the trend of progress about pH probes in cell application in recent years. *Analyst* **2017**, *142* (1), 30–41.
- (28) Kim, H. N.; Lee, M. H.; Kim, H. J.; Kim, J. S.; Yoon, J. A new trend in rhodamine-based chemosensors: application of spirolactam ring-opening to sensing ions. *Chem. Soc. Rev.* **2008**, 37 (8), 1465–1744.
- (29) Beija, M.; Afonso, C. A. M.; Martinho, J. M. G. Synthesis and applications of Rhodamine derivatives as fluorescent probes. *Chem. Soc. Rev.* **2009**, 38 (8), 2410–2433.
- (30) Zhao, X.-X.; Chen, X.-P.; Shen, S.-L.; Li, D.-P.; Zhou, S.; Zhou, Z.-Q.; Xiao, Y.-H.; Xi, G.; Miao, J.-Y.; Zhao, B.-X. A novel pH probe based on a rhodamine—rhodamine platform. *RSC Adv.* **2014**, *4* (92), 50318–50324.
- (31) Shen, S.-L.; Chen, X.-P.; Zhang, X.-F.; Miao, J.-Y.; Zhao, B.-X. A rhodamine B-based lysosomal pH probe. *J. Mater. Chem. B* **2015**, 3 (5), 919–925.
- (32) Wang, L.; Du, W.; Hu, Z.; Uvdal, K.; Li, L.; Huang, W. Hybrid rhodamine fluorophores in the visible/NIR region for biological imaging. *Angew. Chem., Int. Ed.* **2019**, *58* (40), 14026–14043.
- (33) Tena-Solsona, M.; Alonso-de Castro, S.; Miravet, J. F.; Escuder, B. Co-assembly of tetrapeptides into complex pH-responsive

- molecular hydrogel networks. J. Mater. Chem. B 2014, 2 (37), 6192-6197.
- (34) Blum, A. P.; Kammeyer, J. K.; Rush, A. M.; Callmann, C. E.; Hahn, M. E.; Gianneschi, N. C. Stimuli-responsive nanomaterials for biomedical applications. *J. Am. Chem. Soc.* **2015**, *137* (6), 2140–2154.
- (35) Chen, Y. R.; Gan, H. X.; Tong, Y. W. pH-Controlled hierarchical self-assembly of peptide amphiphiles. *Macromolecules* **2015**, *48* (8), 2647–2653.
- (36) Xie, Y.; Wang, X.; Huang, R.; Qi, W.; Wang, Y.; Su, R.; He, Z. Electrostatic and aromatic interaction-directed supramolecular self-assembly of a designed Fmoc-tripeptide into helical nanoribbons. *Langmuir* **2015**, *31* (9), 2885–2894.
- (37) Robin, M. P.; Osborne, S. A. M.; Pikramenou, Z.; Raymond, J. E.; O'Reilly, R. K. Fluorescent block copolymer micelles that can self-report on their Assembly and small molecule encapsulation. *Macromolecules* **2016**, 49 (2), 653–662.
- (38) Shao, H.; Nguyen, T.; Romano, N. C.; Modarelli, D. A.; Parquette, J. R. Self-assembly of 1-D n-type nanostructures based on naphthalene diimide-appended dipeptides. *J. Am. Chem. Soc.* **2009**, 131 (45), 16374–16376.
- (39) Shao, H.; Parquette, J. R. A pi-conjugated hydrogel based on an Fmoc-dipeptide naphthalene diimide semiconductor. *Chem. Commun.* **2010**, *46* (24), 4285–4287.
- (40) Kim, S. H.; Parquette, J. R. A model for the controlled assembly of semiconductor peptides. *Nanoscale* **2012**, *4* (22), 6940–6947.
- (41) Zhao, X. J.; Zhang, S. G. Molecular designer self-assembling peptides. *Chem. Soc. Rev.* **2006**, 35 (11), 1105–1110.
- (42) Zhang, H.; Zheng, X.; Kwok, R. T. K.; Wang, J.; Leung, N. L. C.; Shi, L.; Sun, J. Z.; Tang, Z.; Lam, J. W. Y.; Qin, A.; Tang, B. Z. In situ monitoring of molecular aggregation using circular dichroism. *Nat. Commun.* **2018**, *9* (1), No. 4961.
- (43) Hestand, N. J.; Spano, F. C. Expanded theory of H- and J-molecular aggregates: The effects of vibronic coupling and intermolecular charge transfer. *Chem. Rev.* **2018**, *118* (15), 7069–7163.
- (44) Castelletto, V.; Hamley, I. W.; Cenker, C.; Olsson, U. Influence of salt on the self-assembly of two model amyloid heptapeptides. *J. Phys. Chem. B* **2010**, *114* (23), 8002–8008.
- (45) Derjaguin, B. V.; Churaev, N. V.; Muller, V. M. The Derjaguin—Landau—Verwey—Overbeek (DLVO) Theory of Stability of Lyophobic Colloids. In *Surface Forces*; Springer: US, 1987; pp 293–310
- (46) Cenker, Ç. Ç.; Bucak, S.; Olsson, U. Nanotubes and bilayers in a model peptide system. *Soft Matter* **2011**, 7 (10), 4868–4875.
- (47) Israelachvili, J. N. Effects of Interactions between Aggregates: Mesophases and Multilayers. In *Intermolecular and Surface Forces*, 3rd ed.; Elsevier, 2011; pp 528–530.
- (48) Mei, J.; Leung, N. L.; Kwok, R. T.; Lam, J. W.; Tang, B. Z. Aggregation-induced emission: Together we shine, united we soar! *Chem. Rev.* **2015**, *115* (21), 11718–11940.
- (49) Tanioka, M.; Kamino, S.; Muranaka, A.; Shirasaki, Y.; Ooyama, Y.; Ueda, M.; Uchiyama, M.; Enomoto, S.; Sawada, D. Water-tunable solvatochromic and nanoaggregate fluorescence: dual colour visualisation and quantification of trace water in tetrahydrofuran. *Phys. Chem. Chem. Phys.* **2017**, *19* (2), 1209–1216.
- (50) Li, H.; Hu, D.; Liang, F.; Huang, X.; Zhu, Q. Influence factors on the critical micelle concentration determination using pyrene as a probe and a simple method of preparing samples. *R. Soc. Open Sci.* **2020**, 7 (3), No. 192092.
- (51) Piñeiro, L.; Novo, M.; Al-Soufi, W. Fluorescence emission of pyrene in surfactant solutions. *Adv. Colloid Interface Sci.* **2015**, 215, 1–12
- (52) Vtyurina, N.; Aberg, C.; Salvati, A. Imaging of nanoparticle uptake and kinetics of intracellular trafficking in individual cells. *Nanoscale* **2021**. *13* (23), 10436–10446.
- (53) Arzumanian, V. A.; Kiseleva, O. I.; Poverennaya, E. V. The curious case of the HepG2 cell Line: 40 years of expertise. *Int. J. Mol. Sci.* **2021**, 22 (23), No. 13135.

- (54) Behzadi, S.; Serpooshan, V.; Tao, W.; Hamaly, M. A.; Alkawareek, M. Y.; Dreaden, E. C.; Brown, D.; Alkilany, A. M.; Farokhzad, O. C.; Mahmoudi, M. Cellular uptake of nanoparticles: journey inside the cell. Chem. Soc. Rev. 2017, 46 (14), 4218-4244.
- (55) Kaksonen, M.; Roux, A. Mechanisms of clathrin-mediated endocytosis. Nat. Rev. Mol. Cell Biol. 2018, 19 (5), 313-326.
- (56) Pelkmans, L.; Helenius, A. Endocytosis via caveolae. Traffic 2002, 3 (5), 311-320.
- (57) Yu, Z. L.; Li, W. J.; Liu, F. Y. Inhibition of proliferation and induction of apoptosis by genistein in colon cancer HT-29 cells. Cancer Lett. 2004, 215 (2), 159-166.